

1 **Numerical simulation of atmospheric Lamb waves**
2 **generated by the 2022 Hunga-Tonga volcanic eruption**

3 **Angel Amores¹, Sebastian Monserrat², Marta Marcos^{1,2}, Daniel Argüeso²,**
4 **Joan Villalonga³, Gabriel Jordà³ and Damià Gomis^{1,2}.**

5 ¹Instituto Mediterráneo de Estudios Avanzados (UIB-CSIC), Esporles, Spain.

6 ²Departament de Física (UIB), Palma, Spain.

7 ³Centre Oceanogràfic de Balears, Instituto Español de Oceanografía (IEO-CSIC), Palma, Spain

8 **This manuscript is a non-peer reviewed preprint submitted to EarthArXiv**
9 **that has been submitted to Geophysical Research Letters.**

10 **Key Points:**

- 11 • The underwater Hunga-Tonga volcano exploded generating Lamb waves that trav-
12 eled around the Earth several times.
13 • We simulate these waves using a hydrostatic shallow water equation oceanic model.
14 • The results closely follow the observations of atmospheric pressure perturbations.

Corresponding author: Angel Amores, angel.amores@uib.es

Abstract

On January 15th, 2022, at 4:30 UTC the eruption of the Hunga-Tonga volcano, in the South Pacific Ocean, generated a violent underwater explosion. In addition to tsunami waves that affected the Pacific coasts, the eruption created atmospheric pressure disturbances that spread out in the form of Lamb waves. The associated atmospheric pressure oscillations were detected in high-frequency in-situ observations all over the globe. Here we take advantage of the similarities in the propagation and characteristics between atmospheric Lamb waves and long ocean waves and we use a 2DH ocean numerical model to simulate the phenomenon. We compare the outputs of the numerical simulation with in-situ atmospheric pressure records and with remote satellite observations. The signal in the model matches the observed atmospheric pressure perturbations and reveals an excellent agreement in the wave arrival time between model and observations at hundreds of locations at different distances from the origin.

Plain Language Summary

The underwater explosion of the Hunga-Tonga volcano in the South Pacific Ocean generated atmospheric pressure disturbances, known as Lamb waves, that propagated and surrounded the globe several times. In this study, we exploit the similarities between atmospheric Lamb waves and long waves in the ocean (e.g., tsunamis) to simulate their propagation using an ocean numerical model. The comparison of our results with remote satellite data and in-situ atmospheric pressure records reveals that our model correctly reproduces the propagation of the atmospheric disturbances generated by the volcano explosion.

1 Introduction

On January 14th, 2022 the underwater Hunga-Tonga volcano, located in the South Pacific Ocean, erupted in a one-in-a-thousand year event (Klein, 2022). The volcano, located between the uninhabited islands of Hunga Tonga and Hunga Ha'apai of the Kingdom of Tonga, is part of the Tonga–Kermadec Islands volcanic arc and has been active since its first historical eruption in 1912 (Global Volcanism Program, 2022). The volcano had emerged after an eruption that started in December 2014. This recent eruption resulted in material being deposited and merged with the Hunga Ha'apai island, creating an area of around 2 km of diameter and maximum height of 120 m above sea level (Cronin et al., 2017). According to the Global Volcanism Program (2022), the strongest eruption began on January 15th at 17:30 local time (4:30 UTC) with a plume reaching 30 km in the atmosphere and 600 km in diameter, making it visible by multiple satellite observations. Observations of Sentinel-2 satellites revealed massive changes in the surface area and the disappearance of the formerly deposited volcanic material. The explosive eruption, whose power has been estimated to be equivalent to somewhere between 4 to 18 megatons of TNT (<https://earthobservatory.nasa.gov/images/149367/dramatic-changes-at-hunga-tonga-hunga-haapai>), generated tsunami waves (warnings were issued across several countries in the Pacific coasts) and also atmospheric shock waves that propagated across the globe and were detected by the NASA Aqua satellite as concentric wave patterns (Adam, 2022).

Such amount of energy liberated into the atmosphere by the violent eruption is expected to generate various types of atmospheric waves with different spectral energy content, including inertia gravity waves, infrasound waves or Rossby waves, making the atmospheric wave pattern close to the source very intricate. Among these atmospheric perturbations, the type of wave which is expected to optimally transfer energy over long distances, and therefore the one expected to dominate far away from the source, is the Lamb wave mode, which was first introduced by Horace Lamb (Lamb, 1881). This has been

64 observed in earlier similar events, as for example the well-known Krakatoa volcanic erup-
65 tion in 1883 (Symons, G. J. (ed.), 1888).

66 Lamb waves are non-dispersive atmospheric waves, whose energy is optimally trans-
67 mitted far away from the source with minor losses. They arise as solutions of the mo-
68 mentum equations with zero vertical velocity, meaning that Lamb waves have purely hor-
69 izontal motion, occupying the full depth of the troposphere and with a maximum pres-
70 sure signal at the surface. These waves are only slightly affected by the Earth's rotation
71 and travel at the speed of sound in the media (Gossard & Hooke, 1975). Assuming an
72 isothermal troposphere, the phase velocity of the Lamb waves, C_T , is only affected by
73 the air temperature and is defined as:

$$C_T = \sqrt{\frac{\gamma \cdot R \cdot T}{M}} \quad (1)$$

74 where $\gamma = 1.4$ is the ratio of specific heat of air corresponding to the range of at-
75 mospheric temperatures, $R = 8314.36 \text{ J} \cdot \text{kmol}^{-1} \cdot \text{K}^{-1}$ is the universal gas constant,
76 $M = 28.966 \text{ kg} \cdot \text{kmol}^{-1}$ is the molecular mass for dry air and T is the absolute tem-
77 perature.

78 Due to their particular characteristics, the propagation of Lamb waves through the
79 atmosphere with spatially varying temperature is analog to the behavior of oceanic long
80 waves propagating over an ocean with variable depth. Long waves in the ocean are also
81 non-dispersive barotropic waves traveling with a phase velocity, C_H , given by

$$C_H = \sqrt{g \cdot H} \quad (2)$$

82 where $g = 9.81 \text{ m} \cdot \text{s}^{-2}$ is the gravity acceleration and H is the ocean depth.

83 Long waves in the ocean have been successfully simulated using 2DH shallow wa-
84 ter equation models, as for example, the propagation of tsunami waves and their arrival
85 times at remote coastal locations (e.g. Titov et al. (2005)).

86 Given these similarities between atmospheric Lamb waves and oceanic shallow wa-
87 ter waves, we propose to simulate the atmospheric Lamb wave generated after the Hunga-
88 Tonga volcano explosion using a vertically-integrated hydrodynamic ocean model. To
89 do so, a simple relationship between the vertically integrated atmospheric temperature
90 and the equivalent ocean depth is obtained from eq. 1 and 2

$$H = \frac{\gamma \cdot R \cdot T}{M \cdot g} \quad (3)$$

91 This study is organized as follows: in section 2 the data and the model used for the
92 simulations as well as the way it was initialized are described. Results of the simulations
93 are compared with remote and in-situ observations in section 3 and a summary and con-
94 clusions are presented in section 4.

95 2 Data and Methods

96 The numerical ocean hydrodynamic model SCHISM (Semi-implicit Cross-scale Hy-
97 droscience Integrated System Model, V5.9.0; Y. J. Zhang et al. (2016)) was used to sim-
98 ulate the atmospheric Lamb waves generated by the volcano explosion. We have used
99 its dynamic core, which is a derivative product built from the original SELFE (v3.1dc;
100 Y. Zhang and Baptista (2008)), in 2DH barotropic mode. It solves the vertically-integrated
101 hydrostatic Navier-Stokes equations with shallow water approximation. The model do-
102 main covers the entire globe with an unstructured triangular computational grid of 0.25°
103 resolution with 1036800 nodes and 2070720 elements. The simulation starts on January

15th 2022 at 04:30 UTC coinciding with the volcano explosion and has a duration of 5 days. The computational time step was set to 1 min and the variables were saved every 5 min at each computational grid point.

To define the equivalent water depth in the model (see equation 3), we used the atmospheric temperature fields obtained from ERA5 reanalysis (<https://cds.climate.copernicus.eu/>). ERA5 is a comprehensive reanalysis that spans from 1979 to near-real time and integrates historical observations into global estimates using advanced modeling and data assimilation systems. ERA5 data is provided at 1-hour temporal resolution and 0.25° spatial resolution. A time-varying temperature field over the domain was defined to represent the vertically-averaged atmospheric temperature. For the results shown, the simplest approach was taken. The temperature field has been computed as the average between the temperature at 2 m (obtained from ERA5 data on single levels; Hersbach et al. (2018b)) and the temperature at the top of the troposphere (whose altitude has been taken as constant at 100 hPa level obtained from ERA5 data on pressure levels; Hersbach et al. (2018a)). The results do not vary significantly when more complex algorithm is used to define the temperature field. Tropospheric temperatures were translated into equivalent depth fields using eq. 3, which in turn were incorporated into the model through the bathymetry. As such, the bathymetry field was updated every hour to take into account air temperature variations estimated from ERA5 hourly data.

The initial perturbation created by the volcano eruption was simulated using an equivalent atmospheric pressure perturbation of 50 hPa. In the model, this was introduced as an instantaneous sea level perturbation at the start of the simulation, which had a cylinder-like shape of 60 km radius and 50 cm height. The intensity and the extend of the initial perturbation were chosen to match the amplitude and frequency of the available observations. Other shapes such as a Gaussian and semi-spherical perturbations were also tested for the initial forcing with similar results.

The outputs of the hydrodynamic model are provided as sea surface displacements. We apply the inverted barometer equivalence to convert the sea level response into an atmospheric pressure signal. This approach corresponds to a decrease of 1 hPa for every cm of water elevation, and vice versa. The simulation took a total of 6 h to complete with 23 CPU.

The simulation was validated against in-situ surface atmospheric pressure records obtained from different sources (see the map in Fig. 2 to see the spatial distribution of the stations). A total of 889 station were retrieved from NOAA Automated Surface/Weather Observing Systems (ASOS/AWOS, downloaded from <https://mesonet.agron.iastate.edu/request/asos/1min.phtml#>) spread across all United States, including Hawaii, Alaska and Puerto Rico. From these, only those with less than 10% of missing values were retained, which left a total of 714 stations (20% of them were removed). The time from these stations was described as being UTC. However, some of them showed a time difference with surrounding stations that matched the shift between UTC and local time, which suggests their time record was actually in local time units, thus they were corrected accordingly. Finally, other stations with clear anomalous behavior when compared with surrounding stations were removed. The total number of stations finally used was 660. A time series of atmospheric pressure from Ciutadella (Balearic Islands, Spain) with a temporal resolution of 30 seconds was obtained from the Balearic Islands Coastal Observing and Forecasting System (SOCIB, available at <https://www.socib.es/?seccion=observingFacilities&facility=mooring>). Another time series from Kadhoo (<https://mv.geoview.info/kadhoo,7909905>), in the Maldives, with a 10 minutes temporal resolution was also used to compare with the model outputs. Atmospheric pressure records were also obtained from the Australian Bureau of Meteorology at three locations (Sydney Observatory Hill, Perth Airport and Darwin Airport) with 1 minute temporal resolution. Since the period of the generated Lamb wave was around 40 minutes, the at-

156 atmospheric pressure records were band-pass filtered with cut-off periods between 2 hours
 157 and 15 minutes.

158 The simulation was also qualitatively compared to satellite observations to further
 159 assess the realism of the wave propagation. Infrared data from the Geostationary Op-
 160 erational Environmental Satellite (GOES-R) program (obtained from [https://www.ncdc](https://www.ncdc.noaa.gov/airs-web/search)
 161 [.noaa.gov/airs-web/search](https://www.ncdc.noaa.gov/airs-web/search)) and the European Organisation for Exploitation of Me-
 162 teorological Satellites (EUMETSAT; downloaded from [https://navigator.eumetsat](https://navigator.eumetsat.int/product/EO:EUM:DAT:MSG:HRSEVIRI)
 163 [.int/product/EO:EUM:DAT:MSG:HRSEVIRI](https://navigator.eumetsat.int/product/EO:EUM:DAT:MSG:HRSEVIRI)) were used at 15-min temporal resolution for
 164 the first 24 hours since the eruption. The Pacific region was represented by the GOES-
 165 17 satellite with imagery from the IR10.3 channel with a spatial resolution of 5424×5424
 166 pixels. The 0-degree region was observed by the Meteosat-11 satellite (High Rate SE-
 167 VIRI Level 1.5 Image Data) with data from the IR10.8 channel with a spatial resolu-
 168 tion of 3712×3712 pixels. For the sake of visualization of the atmospheric pressure wave
 169 footprint in the satellite IR observations we used, at each time step, their second time-
 170 derivative. These fields were subsequently spatially filtered with a 50 (100) pixel win-
 171 dows for GOES-17 (Meteosat-11) satellite observations with the filter described in Amores
 172 et al. (2018).

173 3 Results

174 A qualitative comparison of the model results with satellite observations during the
 175 first travel of the Lamb waves (from the origin to the antipodes in Northern Africa) re-
 176 veals that the simulation closely follows the spatial pattern of the satellite measurements
 177 (Fig. 1). Note that we are comparing the observed and modeled spatial footprints of the
 178 waves, but using different variables. The relevant parameter here is thus the location of
 179 the wave rather than its amplitude. Panels *a-f* show the propagation of the Lamb wave
 180 over the Pacific captured by GOES-17 satellite from 15 minutes after the explosion un-
 181 til January 15th 10:30 UTC. The wave is clearly observed in satellite images that also
 182 display a close agreement with the observations. Panels *g-j* show the travel of the wave
 183 captured by Meteosat-11 satellite from 17:30 to 20:30 UTC. In this case, although still
 184 identified, the wave signal is surrounded by noisier data probably due to a larger cloud
 185 coverage and/or lower spatial resolution offered by this satellite in comparison with GOES-
 186 17. The wave is observed at 17:30 and 18:30 and it is still visible at 19:30 and 20:30, co-
 187 inciding again with the pattern of the simulation.

188 Fig. 2 shows the comparison of 10 high-frequency atmospheric pressure records (col-
 189 ors help matching dots in the map and time series in the lower panel) at different dis-
 190 tances from the volcano (indicated with a red star in the map) between January 15th
 191 04:30 UTC until January 18th 02:40 UTC. In addition, the temporal evolution of the sim-
 192 ulation is available in Movie S1 in the Supplementary Material. The modeled time se-
 193 ries (in grey) were extracted from the closer grid point to each station. At all locations
 194 the numerical simulation matches very well the time of arrival of the Lamb wave. At each
 195 site, 4 different passes are observed, except in the Ciutadella station (dark red), the clos-
 196 est to the volcano's antipodes in our database. In this station only two passes occur be-
 197 cause of the overlapping of the northern and southern waves (see Movie S1 for a better
 198 visualization). The model better captures the first wave pass, as shown by both the ar-
 199 rival time and the wave amplitude. Once the Lamb wave has traveled farther distances
 200 and has interfered with its own and the environment, the patterns become more com-
 201 plex. However, the model is still able to correctly capture the arrival time in most cases.

202 Using all available atmospheric pressure records, we have quantified the performance
 203 of the approach by comparing the time of arrival of the first Lamb wave. To do so, we
 204 have determined the time when the first atmospheric pressure maximum is found at in-
 205 situ pressure records and in the model simulation. Fig. 3 represents the scatter plot of
 206 modeled vs. observed arrival times of the first wave. There is an excellent agreement be-

207 tween model and observations at all sites, with a R^2 larger than 0.98 and a root mean
208 square difference (RMSD) of around 10 minutes (we remark here that the temporal res-
209 olution of the simulation is 5 minutes).

210 4 Summary and Conclusions

211 After Hunga-Tonga volcano explosion on January 15th, 2022, atmospheric pressure
212 records around the world measured high-frequency perturbations that traveled around
213 the globe several times and that were consistent with the presence of atmospheric Lamb
214 waves. We have numerically simulated the atmospheric Lamb waves generated by the
215 volcanic eruption taking advantage of their similarities to ocean long waves. Namely, both
216 types of waves propagate through the fluid as vertically integrated waves, with 2D hor-
217 izontal motion and share the same dispersion relation. The analogy consists of defining
218 an equivalent bathymetry in the ocean shallow water model that corresponds to the ver-
219 tically averaged air temperature, which has furthermore temporal variability.

220 The results of the simulation mimic satellite and in-situ observations. In partic-
221 ular, when the outputs of the model are compared to atmospheric pressure records at
222 different distances from the source, they display excellent matching in the arrival times
223 of the perturbation. Therefore, the results confirm that the observed high-frequency sur-
224 face pressure oscillations are the footprint of non-dispersive atmospheric Lamb waves orig-
225 inated by the eruption of the Hunga-Tonga volcano.

226 Despite being an idealized simulation, which neglects various factors that may af-
227 fect different characteristics of the wave, the close agreement between the observation
228 and the model suggests that the main physical mechanisms are well represented in our
229 experiment. For example, our model does not consider the effect of orography. High moun-
230 tain systems such as the Andes or Himalayas may cause reflections of the Lamb waves
231 that are not represented in our simulation. We also made some assumptions in our ap-
232 proach, but they do not prevent us from correctly simulating the wave propagation. For
233 example, we assumed the temperature to be constant in the vertical through the tropo-
234 sphere, but we found that using the average temperature was a good approximation to
235 estimate the equivalent depth. We also assumed the air to be dry and thus, we consid-
236 ered that water vapor and humidity changes have only a minor effect on the propaga-
237 tion of the wave. In summary, we have shown how a vertically integrated hydrodynamic
238 ocean model can be used to investigate and anticipate the propagation of atmospheric
239 Lamb waves across an isotherm troposphere.

240 Conflict of Interest

241 The authors declare no conflicts of interest relevant to this study.

242 Open Research

243 Data Availability Statement: all the data used in this study can be accessed through
244 the links provided in the Data and Methods section.

245 The numerical simulation can be downloaded from: <https://doi.org/10.5281/zenodo.5948860>

246 Acknowledgments

247 This study was supported by the MOCCA project RTI2018-093941-B-C31 funded by MCIN/AEI/
248 /10.13039/501100011033/ and by FEDER Una manera de hacer Europa. It was also sup-
249 ported by grants PGC2018-099285-B-C21 and PGC2018-099285-B-C22 funded by MCIN/AEI/
250 10.13039/501100011033 and by “ERDF A way of making Europe” NextGenerationEU/PRTR.
251 Angel Amores was funded by the Conselleria d’Educació, Universitat i Recerca del Gov-

ern Balear through the Direcció General de Política Universitària i Recerca and by the Fondo Social Europeo for the period 2014–2020 (grant no. PD/011/2019). Daniel Argüeso was funded by Spanish Ministry of Science and Innovation through the EPICC Project (PID2019-105253RJ-I00) and the Beatriz Galindo Programme (BG20/00078). The authors are grateful to NOAA, EUMETSAT, the Australian Bureau of Meteorology and SOCIB to make their data freely available. Finally, we also thank to Dr. Ali Shareef for providing the atmospheric pressure data from the Maldives.

References

- Adam, D. (2022). Tonga volcano eruption created puzzling ripples in earth's atmosphere. *Nature*. doi: 10.1038/d41586-022-00127-1.
- Amores, A., Jordà, G., Arsouze, T., & Le Sommer, J. (2018). Up to what extent can we characterize ocean eddies using present-day gridded altimetric products? *Journal of Geophysical Research: Oceans*, 123(10), 7220-7236. doi: <https://doi.org/10.1029/2018JC014140>
- Cronin, S. J., Brenna, M., Smith, I., Barker, S., Tost, M., Ford, M., ... Vaiomounga, R. (2017). New volcanic island unveils explosive past. *EOS*, 98. doi: <https://doi.org/10.1029/2017EO076589>
- Global Volcanism Program. (2022). Report on hunga tonga-hunga ha'apai (tonga). *Bulletin of the Global Volcanism Network, Smithsonian Institution*, 40:1. doi: <https://doi.org/10.5479/si.GVP.BGVN201501-243040>
- Gossard, E., & Hooke, W. (1975). *Waves in the atmosphere*. Amsterdam: Elsevier.
- Hersbach, H., Bell, B., Berrisford, P., Biavati, G., Horányi, A., Muñoz Sabater, J., ... Thépaut, J.-N. (2018a). Era5 hourly data on pressure levels from 1979 to present. *Copernicus Climate Change Service (C3S) Climate Data Store (CDS)*. doi: 10.24381/cds.bd0915c6
- Hersbach, H., Bell, B., Berrisford, P., Biavati, G., Horányi, A., Muñoz Sabater, J., ... Thépaut, J.-N. (2018b). Era5 hourly data on single levels from 1979 to present. *Copernicus Climate Change Service (C3S) Climate Data Store (CDS)*. doi: 10.24381/cds.adbb2d47
- Klein, A. (2022). Tongan volcano erupts. *New Scientist*, 253(3370), 7. Retrieved from <https://www.sciencedirect.com/science/article/pii/S0262407922000744> doi: [https://doi.org/10.1016/S0262-4079\(22\)00074-4](https://doi.org/10.1016/S0262-4079(22)00074-4)
- Lamb, H. (1881). On the vibrations of an elastic sphere. *Proceedings of the London Mathematical Society*, s1-13(1), 189-212. Retrieved from <https://londmathsoc.onlinelibrary.wiley.com/doi/abs/10.1112/plms/s1-13.1.189> doi: <https://doi.org/10.1112/plms/s1-13.1.189>
- Symons, G. J. (ed.). (1888). The eruption of krakatoa and subsequent phenomena. *Report of the Krakatoa Committee of the Royal Society*.
- Titov, V., Rabinovich, A. B., Mofjeld, H. O., Thomson, R. E., & González, F. I. (2005). The global reach of the 26 december 2004 sumatra tsunami. *Science*, 309(5743), 2045-2048. doi: 10.1126/science.1114576
- Zhang, Y., & Baptista, A. M. (2008). Selfe: A semi-implicit eulerian-lagrangian finite-element model for cross-scale ocean circulation. *Ocean Modelling*, 21(3), 71-96. doi: <https://doi.org/10.1016/j.ocemod.2007.11.005>
- Zhang, Y. J., Ye, F., Stanev, E. V., & Grashorn, S. (2016). Seamless cross-scale modeling with schism. *Ocean Modelling*, 102, 64-81. doi: <https://doi.org/10.1016/j.ocemod.2016.05.002>

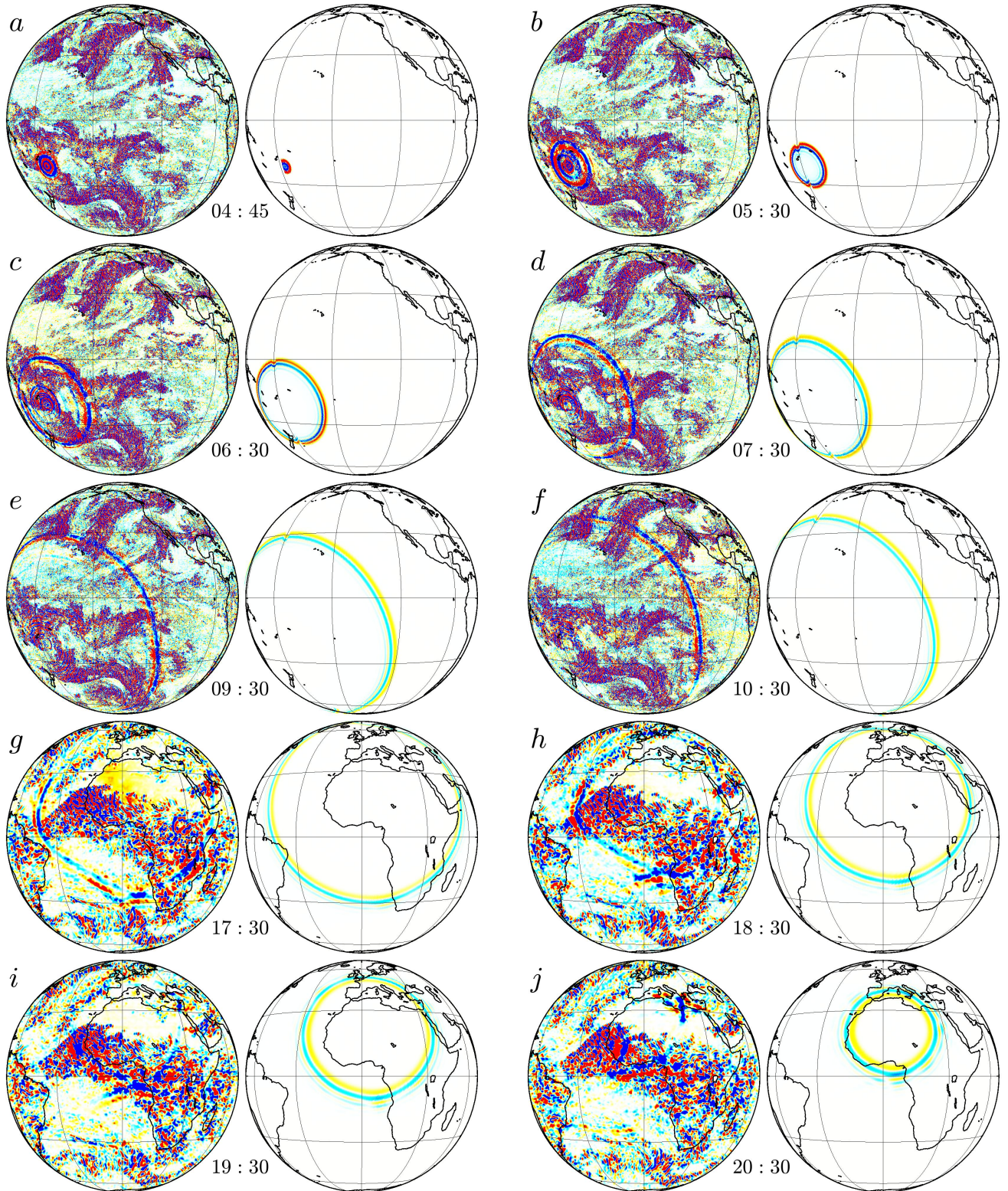


Figure 1. Comparison of the Lamb wave observed from satellite observations and the numerical simulation during January 15th, 2020 at different times. Each panel shows the satellite observations at left and the corresponding simulation field at the right. Panels *a* to *f* correspond to observations from GOES-17 satellite while panels *g* to *j* correspond to observations from Meteosat-11 (see in the Data and Methods sections the details of the postprocessing performed). The colorscales are different for each satellite and numerical simulation and are fixed to provide a correct visualization.

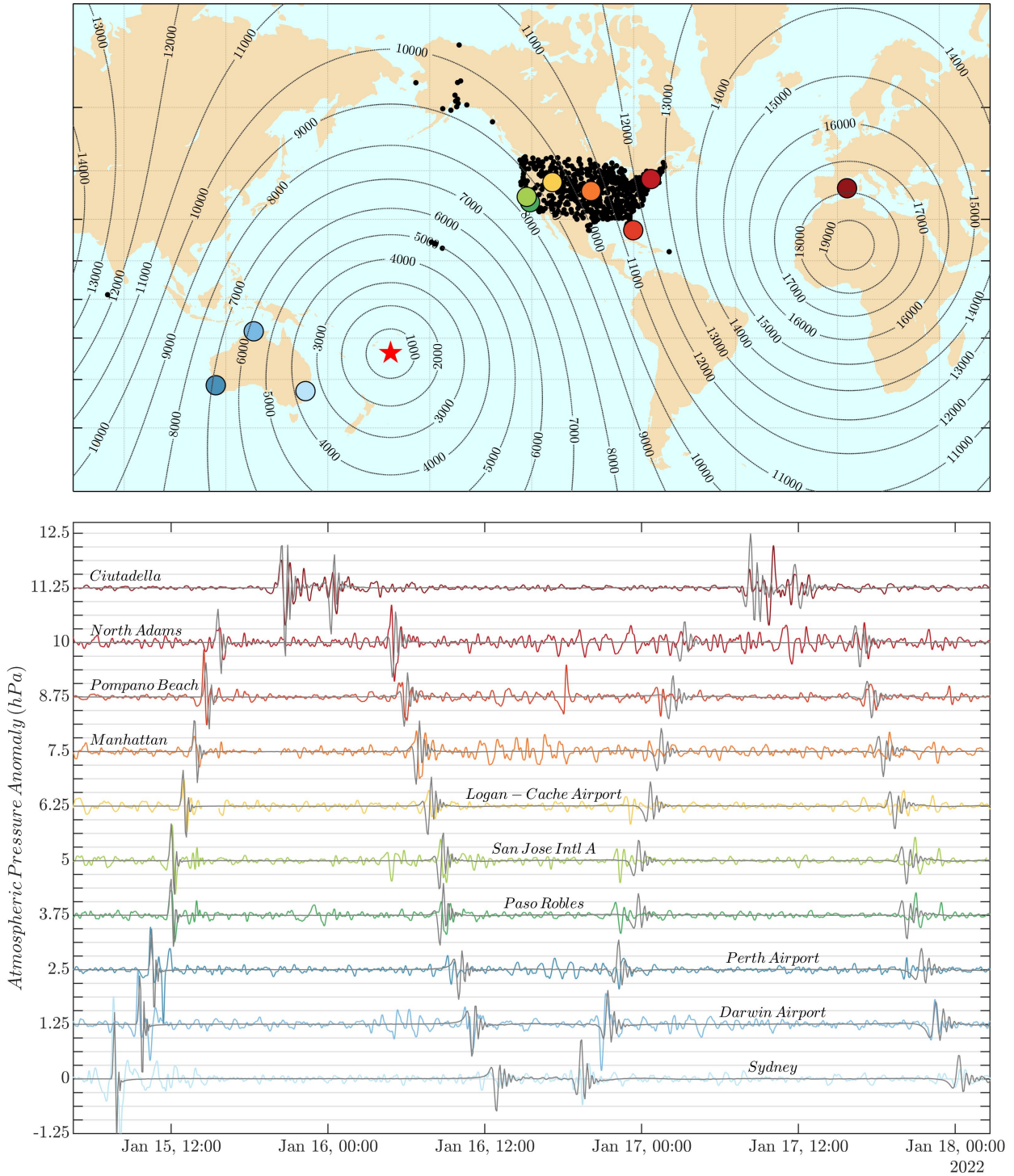


Figure 2. The upper panel shows the location from where all atmospheric pressure records used were measured (black and colored dots). The red star indicated the location of the explosion. Contour lines indicate the distance from the location of the explosion in km. The lower panel shows the comparison between 10 atmospheric pressure anomaly records (in different colors corresponding to the colored points from the upper panel) and the numerical simulation record at the closest grid point (black lines) from January 15th 04:30 UTC until January 18th 02:40 UTC. The different stations shown were selected to cover different distances from the origin of the Lamb wave.

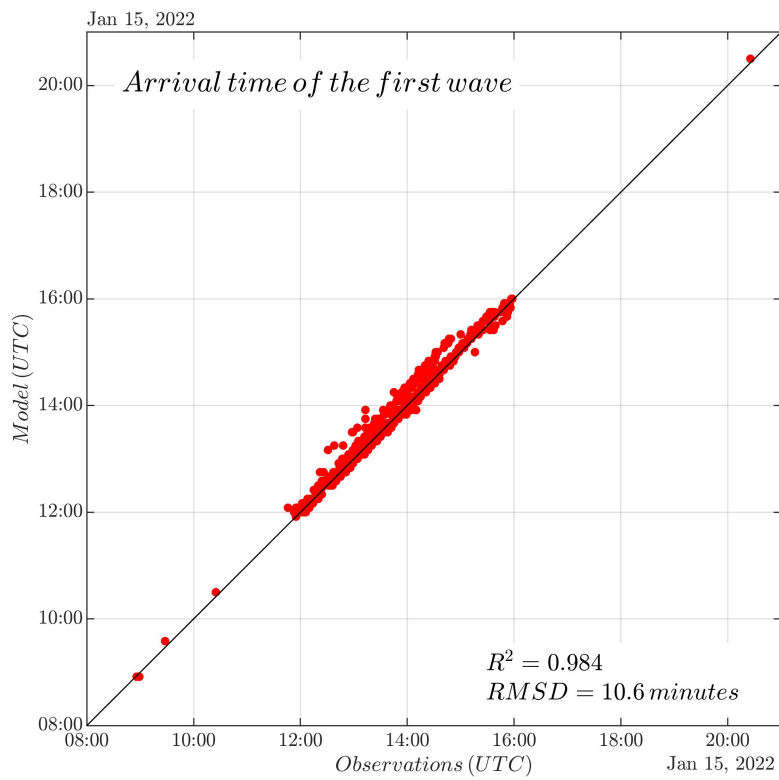


Figure 3. Comparison between the modeled arrival time of the first pass of the Lamb wave as a function of the observed arrival time.